Spin stability of a binary black hole coalescence

C. N. Kozameh[*]
FaMAF, Universidad Nacional de Córdoba 5000, Córdoba, Argentina

G. D. Quiroga[†]
FaMAF, Universidad Nacional de Córdoba 5000, Córdoba, Argentina

(Received 6 June 2020; accepted 14 August 2020; published 8 September 2020)

We analyze the spin stability of a binary black hole coalescence when the binary system is described by the Post-Newtonian (PN) equations in the adiabatic regime. The main idea in this work is to make a massive exploration of the solution space in search of chaos. For that, we evolve the PN equations using a CUDA implementation of the RKF78 scheme and study the dynamical behavior of the system. Each initial spin configuration run in the GPU is composed by more than 80000 simulations. The chaos indicator used to characterize the degree of separation of two infinitesimally close trajectories is the Lyapunov exponent. We find zones in the solution space where the separation between nearby trajectories reaches several orders of magnitude bigger than the initial separation. Also, we note that the chaotic behavior can be observed in forward as well as in backward evolution.

DOI: 10.1103/PhysRevD.102.064015

I. INTRODUCTION

The detection of gravitational waves made by LIGO [1] relies on the filtering of the measured signal to improve the signal-to-noise ratio of the detector. The so-called matched filtering compares the signal with a bank of templates that represent the best theoretical predictions for the expected signal. The theoretical models used to construct these templates are based on Post-Newtonian (PN) and extended PN models. These formalisms link the dynamic variables of the system with the gravitational radiation emitted during the coalescence.

It is then clear that the presence of chaos in the PN equations of motion that describe the coalescence of spinning black holes (BH) translates into a huge enlargement of the parameter space needed for a matching algorithm. In fact, it has been shown by several authors that chaos does appear in the inspiral time of a coalescing system [2–7]. Therefore, a high accurate parameter estimation (component masses, sky location, distance, etc.) of gravitational waves requires computing millions of waveforms. Otherwise, the presence of chaos in the system can lead to an incorrect parameter and uncertainties in predicting initial configurations. Thus, the study of chaos during the inspiral time using a massive exploration of the solution space is required in order to improve the PN models and parameter estimates.

Another place where chaos may be present before the inspiral time is in the quasicircular or adiabatic regime. In this case, one asks whether or not the system may become chaotic before the frequency of revolution reaches the maximum level compatible with the quasicircular assumption. An effective time $t_m = 2\pi/\omega_{\max}$ can be used to check whether the system becomes chaotic even in the circular phase. Any chaotic behavior in this regime will also be present in the final inspiral period, and it can greatly reduce the possibility of detection even with templates that include spin effects. It is thus important to study the stability of the spins in the adiabatic regime of the BH binary.

In this work, we address this issue using a suitable PN model that describes quasicircular or adiabatic orbits. It is worth mentioning that in our setup we describe the orbital plane using the Newtonian angular momentum $\vec{L}_N = \vec{r} \times m\vec{v}$ since $\vec{L}_N$ is perpendicular to the orbital plane for circular orbits. Although in Hamiltonian formulations, the orbital angular momentum $\vec{L} = \vec{r} \times \vec{p}$ is a more useful object to describe the orbital plane; in our case, we are following an ansatz that uses $\vec{L}_N$ as one of the auxiliary variables in the ODEs with a geometrical meaning.

We take advantage of the performance of Nvidia GPUs in order to accelerate the intensive exploration of the parameter space looking for chaos in the PN equations that describe the BH-BH coalescence. For this, we introduce a new numerical code written in CUDA-C [8], which can solve the PN system of ordinary differential equations (EDOs) for a large set of initial conditions. One of the benefits of our approach is that the numerical implementation will have the basic infrastructure of a competitive code, which can be subsequently generalized to include extended PN models like the "effective one body" (EOB), which is more accurate to describe binary coalescence and the

---

[*] kozameh@famaf.unc.edu.ar
[†] gquiroga@famaf.unc.edu.ar

emitted radiation [9–11]. The basic idea, in this first paper, is to focus on studying chaos of binary BHs for different initial spin configurations and mass ratios. The coalescence will be described by PN formalism in the adiabatic regime, and the indicator used to characterize chaos will be the Lyapunov coefficient, defined as the divergence rate between initially nearby trajectories,

$$\lambda(t) = \frac{1}{t}\ln\left(\frac{|\Delta Y(t)|}{|\Delta Y(0)|}\right). \tag{1}$$

In the above formula, ΔY between two points in phase space is simply the Cartesian distance between the dimensionless six-component coordinate vectors $[S_{1i}, S_{2j}]$ and $[S'_{1i}, S'_{2j}]$ of two nearby trajectories. In our numerical integrations, the initial separation is a small displacement in phase space with a random orientation and a magnitude of $\Delta Y(0) = 10^{-9}$. The two trajectories are then integrated forward in time, recording the separation $\Delta Y(t)$, from which $\lambda(t)$ is computed. In chaotic systems, the divergence will be exponential in time with a roughly constant (positive) exponent. We define the Lyapunov time $t_L \equiv 1/\lambda$ as the time scale on which nearby trajectories separate by a factor of e. This Lyapunov time can be computed for the problem of coalescing compact binaries in quasicircular orbits and compared with the relevant time scale $t_m = 2\pi/\omega_{\max}$. Thus, if $t_m \ll t_L$, chaos will not affect the dynamics, whereas if $t_L \geq t_m$, the system will be chaotic. We numerically integrate the PN equations up to t_m and show that for extremely large regions in parameter space the system is chaotic. We conclude that in general, the quasicircular binary system will exhibit chaotic behavior, and a huge number of parameters must be used to adequately define the templates for any system of wave extraction.

Another issue worth pursuing is whether or not the presence of 3.5PN terms in the evolution equations for the particular case of only one spinning binary produces chaotic behavior. Let us recall that at the 2PN level, the Hamiltonian equations of motion are integrable [12]. Thus, there is no chaos in the evolution of these solutions. We perform a similar evolution in our equations and find several nice results that are presented in this work.

Finally, we also address the following question. Given a set of coordinates in parameter space at t_m that describe the binary system at that time, how many different conditions in the past were such that they produce the same present state (up to an experimental error) of the observed orbits and spins? This is a standard problem in meteorology if one replaces the binary system by the weather data at a given day and one wants to know how many different weather conditions in the past were able to produce that particular observed data. In binary coalescence, this is also an important issue. In many cases, one computes the final spin of the resulting black hole of the system as the initial intrinsic angular momentum of the system plus an integral of a suitable expression from $-\infty$ to the final stationary black hole, usually defined at $+\infty$. To answer this question, we integrate the PN equations backwards in time and show that the system is also chaotic.

This article is organized as follows, in Sec. II, the PN equations are introduced. In Sec. III, the CUDA implementation of the Runge-Kutta-Fehlberg scheme is shown, and also we discuss about the code architecture. In Secs. IV and V, the simulation setup and the main results are presented, respectively. Finally, we close the work, giving some final remarks and conclusions.

II. PN EQUATIONS

The PN equations are an approximation of the two-body problem in general relativity (GR), which essentially involves expansions in terms of quotients of the ratio v/c. Like the newtonian two-body problem, it is possible in the PN approach to describe the motion of a binary system from its center of mass. However, this approach depends on the initial configuration of the black holes. A general state of this topic is described by Luc Blanchet in the following reference [13].

In this paper, we restrict our analysis to the adiabatic regime where the inspiral of the compact objects can be represented as a sequence of quasicircular orbits. The numerical evolution is made using CUDA and GPU; the equations evolved are written up to 3.5PN order in the angular frequency ω and also up to 2PN order in spin effects [14,15]. In this approach, the black holes are assumed to follow quasicircular orbits, which correspond to orbits that would be exactly circular, that is, of a constant radius r in the absence of spin and gravitational radiation. The coupled PN equation system is expressed in terms of the masses, and the orbital frequency ω notes that the validity of this formalism can be extended at the limit $\omega_{\max} = 0.05$ [16,17]. Thus, this limit will be introduced as a stop condition in our simulations, and it also useful to define a maximum time $t_m \equiv 2\pi/\omega_{\max}$.

First, we introduce the mass ratios and some needed constants,

$$M = m_1 + m_2, \tag{2}$$

$$\eta = \frac{m_1 m_2}{(m_1 + m_2)^2}, \tag{3}$$

$$\delta = \frac{m_1 - m_2}{m_1 + m_2}, \tag{4}$$

$$\theta_N = \frac{1039}{4620}, \tag{5}$$

$$\gamma_E = 0.577215664901532860606, \tag{6}$$

where γ_E is the is Euler's constant. The separation r between the two black holes in the quasicircular approach [18] is given by

$$M\omega = \left(\frac{M}{r}\right)^{3/2}. \tag{7}$$

The evolution equations for the spin vectors of each black hole S_1, S_2, the unit Newtonian angular momentum vector $\hat{\mathbf{L}}_N$, and the orbital frequency are written in geometrized units ($G = c = 1$) as follows:

(i) Precession equations for the spins,

$$\dot{\mathbf{S}}_1 = \mathbf{\Omega}_1 \times \mathbf{S}_1, \tag{8}$$

$$\dot{\mathbf{S}}_2 = \mathbf{\Omega}_2 \times \mathbf{S}_2, \tag{9}$$

where

$$\mathbf{\Omega}_1 = \frac{(M\omega)^2}{2M}\left(\eta(M\omega)^{-1/3}\left(4 + 3\frac{m_2}{m_1}\right)\hat{\mathbf{L}}_N + M^{-2}(\mathbf{S}_2 - 3(\mathbf{S}_2 \cdot \hat{\mathbf{L}}_N)\hat{\mathbf{L}}_N)\right), \tag{10}$$

and $\mathbf{\Omega}_2$ is obtained exchanging $1 \leftrightarrow 2$.

(ii) The evolution equation for the Newtonian angular momentum, which comes from $\dot{J} = 0$, can be written as

$$\dot{\hat{\mathbf{L}}}_N = -\frac{(M\omega)^{1/3}}{\eta M^2}(\dot{\mathbf{S}}_1 + \dot{\mathbf{S}}_2). \tag{11}$$

(iii) The orbital frequency equation is given by

$$\begin{aligned}\dot{\omega} = \omega^2 \frac{96}{5}\eta(M\omega)^{5/3}\Bigg\{&1 - \frac{743 + 924\eta}{336}(M\omega)^{2/3} - \left(\frac{1}{12}\sum_{i=1,2}\left[\frac{1}{m_i^2}\hat{\mathbf{L}}_N \cdot \mathbf{S}_i\left(\frac{113m_i^2}{M^2} + 75\eta\right)\right] - 4\pi\right)M\omega \\ &+ \left(\frac{34103}{18144} + \frac{13661}{2016}\eta + \frac{59}{18}\eta^2\right)(M\omega)^{4/3} - \frac{1}{48}\frac{\eta}{m_1^2 m_2^2}[247(\mathbf{S}_1 \cdot \mathbf{S}_2) - 721(\hat{\mathbf{L}}_N \cdot \mathbf{S}_1)(\hat{\mathbf{L}}_N \cdot \mathbf{S}_2)](M\omega)^{4/3} \\ &- \frac{1}{672}(4159 + 15876\eta)\pi(M\omega)^{5/3} + \Bigg[\left(\frac{16447322263}{139708800} - \frac{1712}{105}\gamma_E + \frac{16}{3}\pi^2\right) \\ &+ \left(-\frac{273811877}{1088640} + \frac{451}{48}\pi^2 - \frac{88}{3}\hat{\theta}\eta\right)\eta + \frac{541}{896}\eta^2 - \frac{5605}{2592}\eta^3 - \frac{856}{105}\log(16(M\omega)^{2/3})\Bigg](M\omega)^2 \\ &+ \left(-\frac{4415}{4032} + \frac{358675}{6048}\eta + \frac{91495}{1512}\eta^2\right)\pi(M\omega)^{7/3}\Bigg\}.\end{aligned} \tag{12}$$

(iv) Finally, the accumulated orbital phase is given by

$$\Psi = \int_{t_0}^{t} \omega dt = \int_{\omega_0}^{\omega} \frac{\omega}{\dot{\omega}} d\omega. \tag{13}$$

This phase describes the position of the two compact objects along the instantaneous circular orbits of the adiabatic sequence.

At any point along the inspiral, the binary is completely described by the orbital angular frequency ω, the orbital phase Ψ, the direction $\hat{\mathbf{L}}_N$ of the orbital angular momentum, and the two spins $\mathbf{S}_1$ and $\mathbf{S}_2$.

III. INTRODUCING THE OMEGA–CUDA CODE

In order to solve the system of ordinary differential equations (ODEs) described by Eqs. (8), (9), (11), and (12), we implement a numerical method of the Runge-Kutta (RK) family [19].

Our general code, named Omega-CUDA, contains the following methods of the RK family: the traditional Runge-Kutta (RK4), the Dormand-Prince scheme (DP45) [20], and the Runge-Kutta-Fehlberg (RKF78) used as one of the main methods of MATLAB [21].

However, in this article, all the numerical simulations are performed using the RKF78. For this reason, its implementation in Omega-CUDA is discussed below.

The RKF78 is an explicit and embedded method of the seventh order, with an adaptive step, which allows for validating the integration step using an eighth order estimation for the error. In the RKF78 algorithm, ten coefficients are calculated for the seventh order and twelve coefficients for the highest order solutions. In our code, all the mentioned methods are implemented in the kernel of the GPU; thus, some modification was introduced in order to make a massive parallelization to keep a good performance without affecting the output data, ensuring the same length and the same step size for each initial condition.

A. Omega-CUDA architecture

CUDA is a parallel computing platform introduced by NVidia in 2006 [22]; this leverages the parallel compute

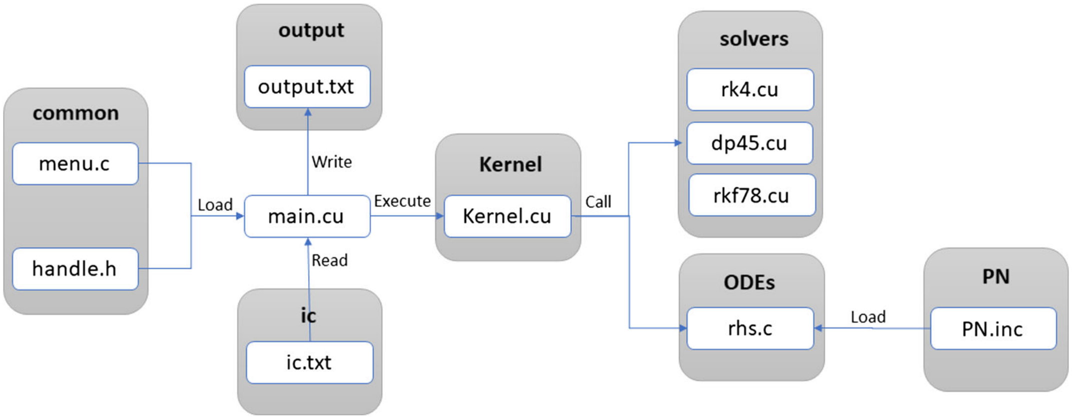

FIG. 1. This figure shows the architecture of Omega-CUDA; the gray blocks represent the folders where the files are located. For simplicity, some headers are not included in the diagram.

engine in video cards to solve many complex computational problems with a higher performance than the traditional CPU codes. The CUDA architecture allows developing codes in familiar languages such as C/C++, Fortran, and PYTHON among others.

Omega-CUDA is a GPUPU code inspired by two previously published codes [23,24]; its basic structure is shown in the following Fig. 1,

The initial conditions are stored in a text file (ic.txt) as an array of $10 \times N$, where N is the desired number of independent initial configurations or PN systems. The file is arranged as follows:

ω	S_{1x}	S_{1y}	S_{1z}	S_{2x}	S_{2y}	S_{2z}	$\hat{L}_{Nx}$	$\hat{L}_{Ny}$	$\hat{L}_{Nz}$
⋮	⋮	⋮	⋮	⋮	⋮	⋮	⋮	⋮	⋮

On the other hand, the output file is an ASCII flat text, where all the generated data during the integration is stored; this file will be created in the output folder in the following format:

τ	ω	S_{1x}	S_{1y}	S_{1z}	S_{2x}	S_{2y}	S_{2z}	$\hat{L}_{Nx}$	$\hat{L}_{Ny}$	$\hat{L}_{Nz}$	
0	ω_0^1	S_{1x0}^1	S_{1y0}^1	S_{1z0}^1	S_{2x0}^1	S_{2y0}^1	S_{2z0}^1	$\hat{L}_{Nx0}^1$	$\hat{L}_{Ny0}^1$	$\hat{L}_{Nz0}^1$	1st PN-system at $\tau = 0$
0	ω_0^2	S_{1x0}^2	S_{1y0}^2	S_{1z0}^2	S_{2x0}^2	S_{2y0}^2	S_{2z0}^2	$\hat{L}_{Nx0}^2$	$\hat{L}_{Ny0}^2$	$\hat{L}_{Nz0}^2$	2nd PN-system at $\tau = 0$
h	ω_h^1	S_{1xh}^1	S_{1yh}^1	S_{1zh}^1	S_{2xh}^1	S_{2yh}^1	S_{2zh}^1	$\hat{L}_{Nxh}^1$	$\hat{L}_{Nyh}^1$	$\hat{L}_{Nzh}^1$	1st PN-system at $\tau = h$
h	ω_h^2	S_{1xh}^2	S_{1yh}^2	S_{1zh}^2	S_{2xh}^2	S_{2yh}^2	S_{2zh}^2	$\hat{L}_{Nxh}^2$	$\hat{L}_{Nyh}^2$	$\hat{L}_{Nzh}^2$	2nd PN-system at $\tau = h$
⋮	⋮	⋮	⋮	⋮	⋮	⋮	⋮	⋮	⋮	⋮	⋮

Here, the superscript indicates the PN system, and the extra subscript refers to the integration step. The numerical implementation made in Omega-CUDA allows us to solve a large set of systems independently; this code can be downloaded from the following git repository: https://github.com/GonzaQuiro/Omega-CUDA.

The Omega-CUDA code is designed to integrate the full set of initial conditions from $t = t_0 = 0$ to the final time $t = t_f$ chosen by the user. However, it is important to note that there is a stop condition in the CUDA kernel which must be verified for each independent thread in order to ensure the validity of the integration. Since the PN equations still hold at $\omega = \omega_{\max} = 0.05$, when a system reaches this limit, the execution of this thread stops and returns the last value before reaching $\omega_{\max}$ in time t_m. Thus, this particular thread goes between t_0 and $t_m \leq t_f$ before the integration ends.

IV. SIMULATION SETUP

In this section, we will give some details concerning the simulations and the coefficient used as indicator in the data analysis. First, we must remember that the Eqs. (8), (9), (11), and (12) are solved using the RKF78 method with a tolerance $\epsilon = 10^{-10}$ with a step size $h = 0.1$, and assuming the total mass $M = 1$ as is usual in the numerical practices.

The initial data stored in ic.txt file contain 80802 initial conditions, which correspond to 40401 points in the diagrams introduced in the next section. These points are computed using the initial conditions $\mathbf{y}$ and a perturbation $\mathbf{y}+\delta\mathbf{y}$, where $\delta\mathbf{y}$ is the initial separation in the solution space, which is set to $O(10^9)$.

On the other hand, we introduce the following Euclidean norm in order to measure distance between the system and its perturbation:

$$||\Delta\mathbf{y}(t)||^2 = \sum_{i=1}^{2} [(S_{ix(\mathbf{y})} - S_{ix(\mathbf{y}+\delta\mathbf{y})})^2 + (S_{iy(\mathbf{y})} - S_{iy(\mathbf{y}+\delta\mathbf{y})})^2 + (S_{iz(\mathbf{y})} - S_{iz(\mathbf{y}+\delta\mathbf{y})})^2] \\ + (\hat{L}_{Nx(\mathbf{y})} - \hat{L}_{Nx(\mathbf{y}+\delta\mathbf{y})})^2 + (\hat{L}_{Ny(\mathbf{y})} - \hat{L}_{Ny(\mathbf{y}+\delta\mathbf{y})})^2 + (\hat{L}_{Nz(\mathbf{y})} - \hat{L}_{Nz(\mathbf{y}+\delta\mathbf{y})})^2 \\ + (\omega_{(\mathbf{y})} - \omega_{(\mathbf{y}+\delta\mathbf{y})})^2. \tag{14}$$

In our simulations, the initial angular momentum $\hat{\mathbf{L}}_N = [0, 0, 1]$ and the orbital frequency $\omega = 0.01$ will remain fixed, but we will vary the initial configurations of the BHs spin. These configurations sweep over two spin components, while the rest remains fixed. For instance, an input file will look like

ω	S_{1x}	S_{1y}	S_{1z}	S_{2x}	S_{2y}	S_{2z}	$\hat{L}_{Nx}$	$\hat{L}_{Ny}$	$\hat{L}_{Nz}$	$\mathbf{y}$
0.01	−1.0000000000	−1.000000000	1.0	0.0	−1.0	1.0	0.0	0.0	1.0	$\mathbf{y}_1$
0.01	−0.9999999990	−0.9999999990	1.0	0.0	−1.0	1.0	0.0	0.0	1.0	$\mathbf{y}_1+\delta\mathbf{y}$
0.01	−1.0000000000	−0.9900000000	1.0	0.0	−1.0	1.0	0.0	0.0	1.0	$\mathbf{y}_2$
0.01	−0.9999999990	−0.9899999990	1.0	0.0	−1.0	1.0	0.0	0.0	1.0	$\mathbf{y}_2+\delta\mathbf{y}$
⋮	⋮	⋮	⋮	⋮	⋮	⋮	⋮	⋮	⋮	⋮

Now, we will introduce some indicators which are used to make the data analysis and compare the separation between $\mathbf{y}$ and $\mathbf{y}+\delta\mathbf{y}$. One way to perform this task is by using the deviation vector method in order to compute the Lyapunov coefficients.

The exponents of Lyapunov are quantities that characterize the degree of separation of two infinitesimally close trajectories; this is a method widely used to study chaos in dynamic systems. Particularly, the maximal Lyapunov exponent λ is an indicator of chaos in an ODE system. The maximum exponent of Lyapunov for an orbit starting at $\mathbf{y}$ and a near orbit $\mathbf{y}+\delta\mathbf{y}$ is defined by the equation [25],

$$\lambda = \lim_{t\to\infty} \frac{1}{t} \ln \frac{||\Delta\mathbf{y}(t)||}{||\Delta\mathbf{y}(t_0)||}. \tag{15}$$

Here, $\Delta\mathbf{y}(t)$ corresponds to the vector deviation between the orbits and $||\Delta\mathbf{y}(t)||$ is the Euclidian norm given by Eq. (14). Then a negative Lyapunov exponent is synonymous with stability, while a positive λ is a characteristic of chaos [26].

In practice, there are several numerical implementations, which can be used to compute the maximal Lyapunov exponent [27]. One of the most extended is comparing $\ln \frac{||\Delta\mathbf{y}(t)||}{||\Delta\mathbf{y}(t_0)||}$ vs t; such a plot should be approximately linear, and the slope of this curve is equal to the principal Lyapunov exponent. The slope can be extracted just performing a least-squares fit to the simulation data. In our PN systems, some consideration must be taken account; first, $w \le w_{\max}$, and second, the norm $||\delta\mathbf{y}|| \le 10^{-2}$ in order to avoid the saturation problem in this method.

However, this method is too expensive computationally speaking and cannot be applied directly in the forward evolution since the time in which PN formalism is valid is too short, around 70 yr. Also, the λ exponents are too small, hindering the identification of the zones where there is a big separation of the trajectories. So, in practice, instead of the Lyapunov exponents, we use the ratio Q in the forward evolution defined as (15),

$$Q(t) \equiv \frac{||\Delta\mathbf{y}(t)||}{||\Delta\mathbf{y}(t_0)||}. \tag{16}$$

We now define the Lyapunov time $t_L \equiv 1/\lambda$ as the time scale on which nearby trajectories separate by a factor of e, i.e., $Q(t_L) = e$. We then compare the Lyapunov time with a characteristic time for the problem of coalescing compact binaries in quasicircular orbits. In this case, the relevant time scale is $t_m = 2\pi/\omega_{\max}$. Thus, if $t_m \ll t_L$, chaos will not affect the dynamics, whereas if $t_L \ge t_m$, the system will be chaotic. We numerically integrate the PN equations up to t_m and plot $Q(t_m)$ for extremely large regions in parameter space. Any region with $Q(t_m) \ge e$ yields evidence of chaotic behavior.

V. MAIN RESULTS

A. Forward evolution

We present here the simulation results and show the main plots of this article. As was discussed in the previous section, the ratio $Q(t_m)$ (16) is plotted for different configurations of S_{1x} vs S_{1y} and also S_{1x} vs S_{2y}. The different regions are colored with the visible light spectrum. The red zone in the figures are regions where $||\Delta\mathbf{y}(t_m)||$ is 2 or higher orders of magnitude bigger than the initial separation $||\Delta\mathbf{y}(t_0)||$, whereas the deep violet regions represent a value of Q less than e.

The following four figures (Figs. 2 and 3) show the same spin configurations with a different mass ratio; the initial spins are chosen as $S_1 = [S_{1x}, S_{1y}, 1], S_2 = [1, 0, -1]$.

Here, S_{1x}, S_{1y} and S_{2x}, S_{2y} always vary between $[-1, 1]$, with a separation of 0.01.

The red zones indicate that these spin configurations are markedly far between the initial time and t_{ω_c}, which corresponds to the validity time where the PN equations still holds. On the other hand, some red strips can also be observed when the ratio mass is changing. Note also that almost all regions in the figures show chaotic behavior since there is hardly any place with deep violet. The situation presented above corresponds to two black holes that do not belong to the same stellar evolution since the spins are completely misaligned.

We now turn our attention to more symmetric situations. For that, we restrict ourselves to an equal mass configuration and just change the relative alignment between the z component of the BHs spin as we show in the following figure (Fig. 4),

Here, we can see a clear difference between the antialigned (Fig. 4 left) and the aligned configurations (Fig. 4 right). Whereas the antialigned case is chaotic except for a narrow band, there is a broad region in solution space with nonchaotic behavior when the spins are aligned.

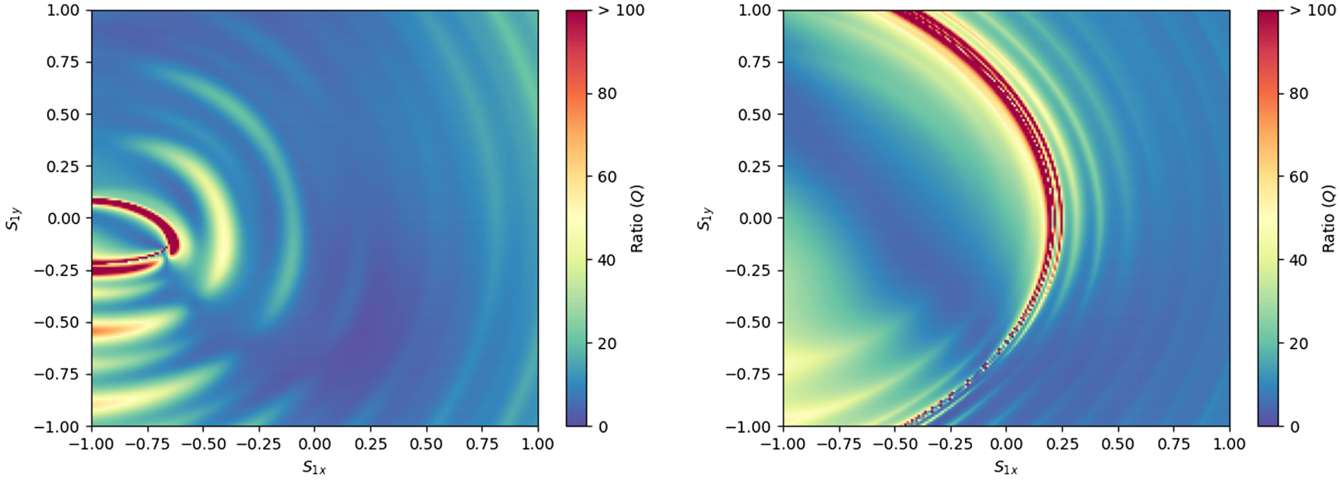

FIG. 2. The figures show the same initial spin configurations with a mass $m_1 = 0.7$, $m_2 = 0.3$ in the left figure, and $m_1 = 0.5$, $m_2 = 0.5$ in the right one. In both plots, we "sweep" over S_{1x} and S_{1y}, keeping the remaining components fixed.

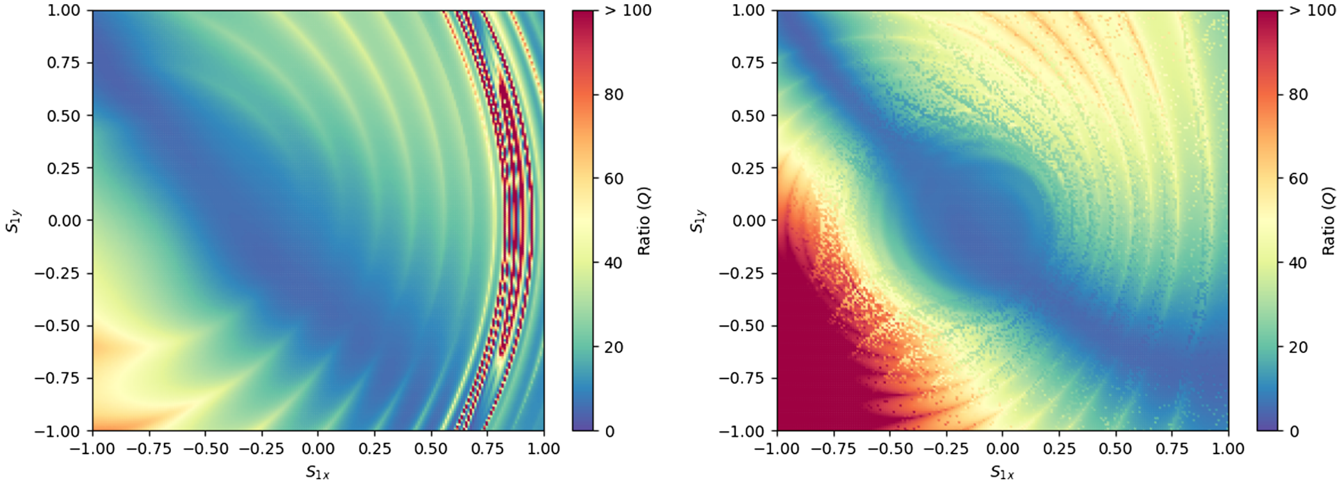

FIG. 3. These figures show the same previous initial configuration assuming $m_1 = 0.4$, $m_2 = 0.6$ and $m_1 = 0.3$, $m_2 = 0.7$, respectively.

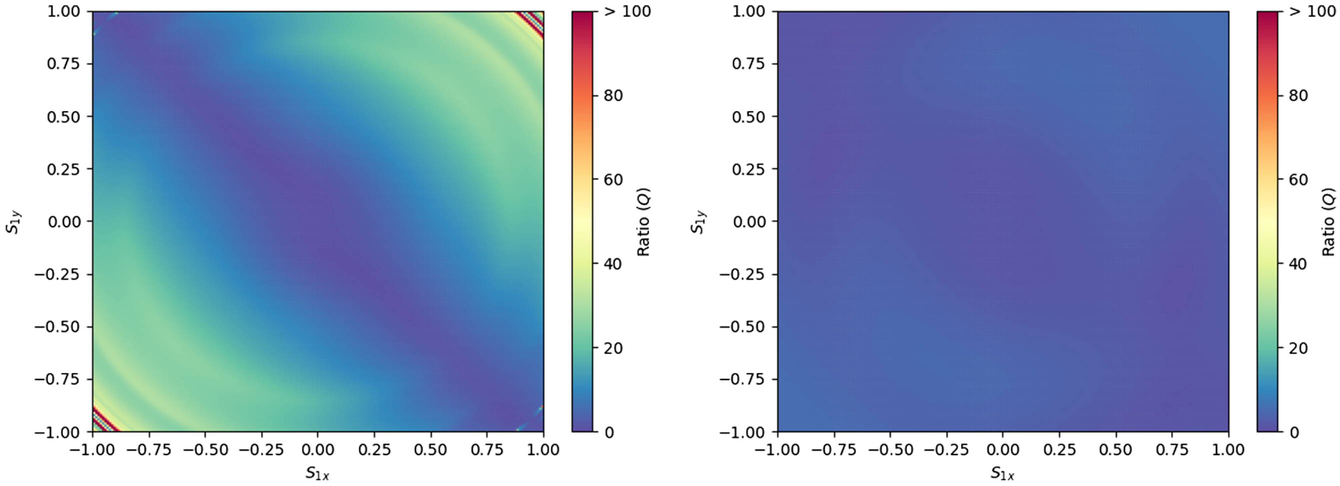

FIG. 4. These figures show the separation between two between two trajectories. The initial spin configurations are $S_1 = [S_{1x}, S_{2y}, 1]$, $S_2 = [0, 0, -1]$ for the right plot and $S_1 = [S_{1x}, S_{2y}, -1]$, $S_2 = [0, 0, -1]$ for the left.

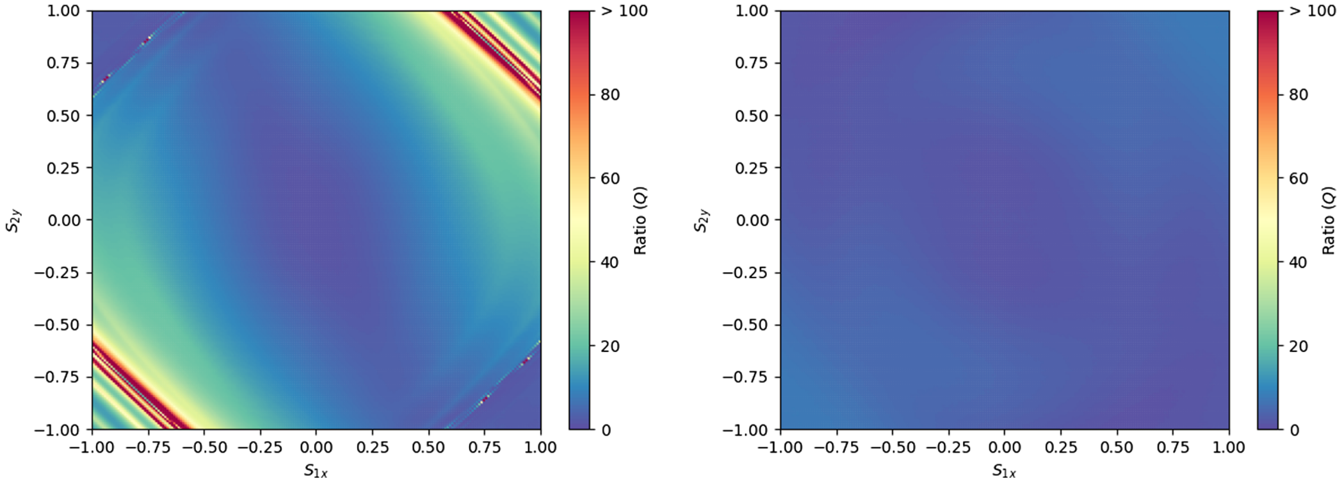

FIG. 5. Plots for the spin configurations $S_1 = [S_{1x}, S_{2y}, 1]$, $S_2 = [0, -1, -1]$ for the right plot and $S_1 = [S_{1x}, S_{2y}, -1]$, $S_2 = [0, -1, -1]$ for the left.

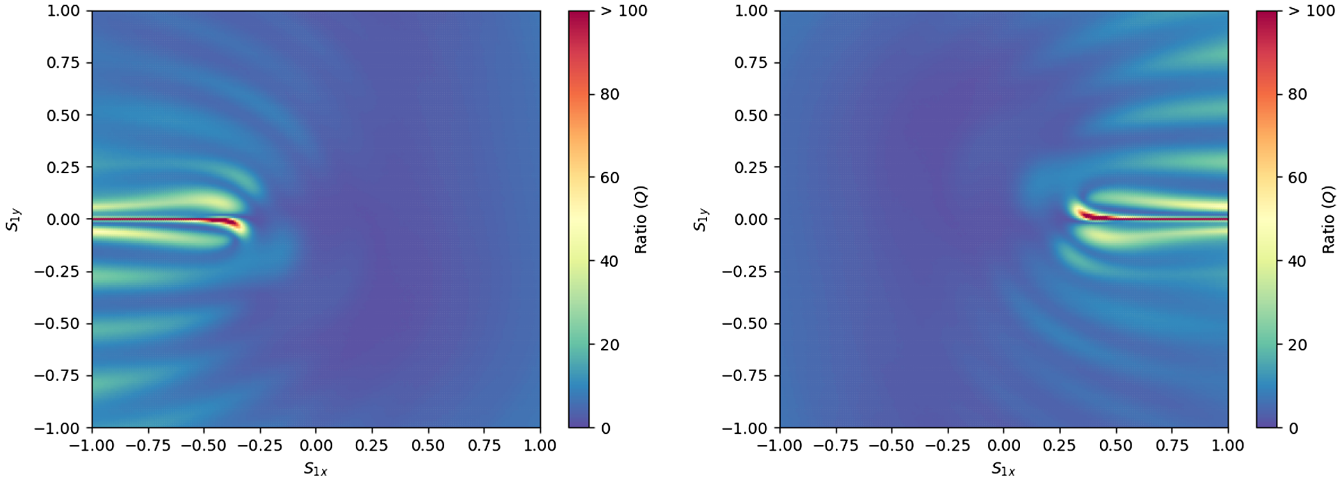

FIG. 6. In the left figure, $S_1 = [S_{1x}, S_{2y}, 0]$, $S_2 = [1, 0, 0]$, and the right figure is started with $S_1 = [S_{1x}, S_{2y}, 0]$, $S_2 = [-1, 0, 0]$.

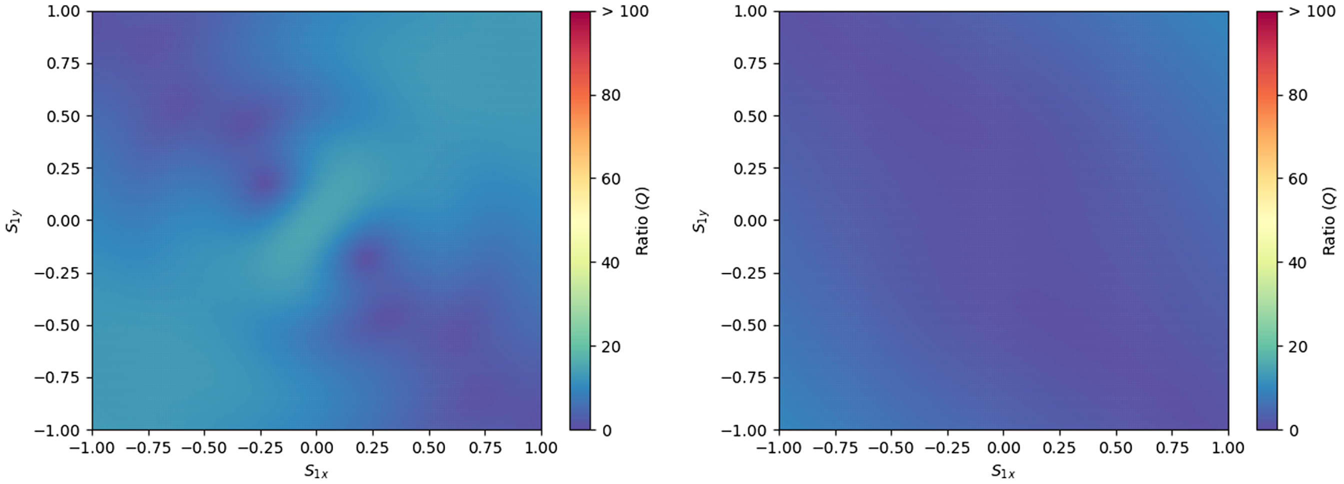

FIG. 7. In both figures $S_2 = 0$, with the initial orientation of S_{1z} aligned (left figure) or antialigned (right figure) with L_z.

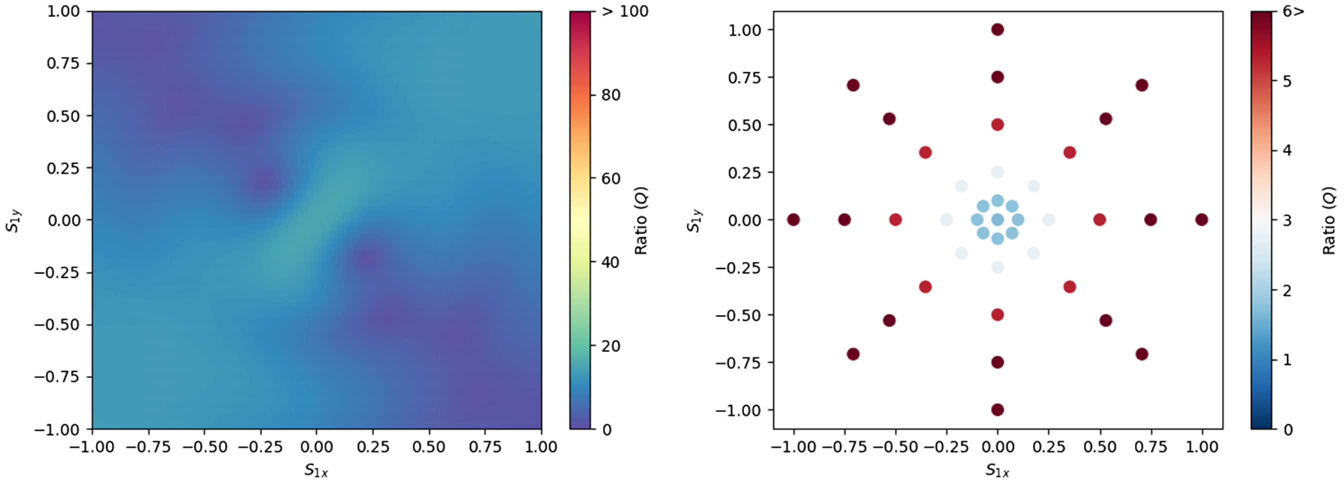

FIG. 8. Q coefficient for one spinning black hole. On the left, we plot the configuration $S_1 = [S_{1x}, S_{1y}, 0]$, $S_2 = 0$. On the right, we plot a rotation around the point (0, 0) for the previous configuration $S_{1z} = 0$, where the perturbations are aligned with the S_{1x}, S_{1y} direction.

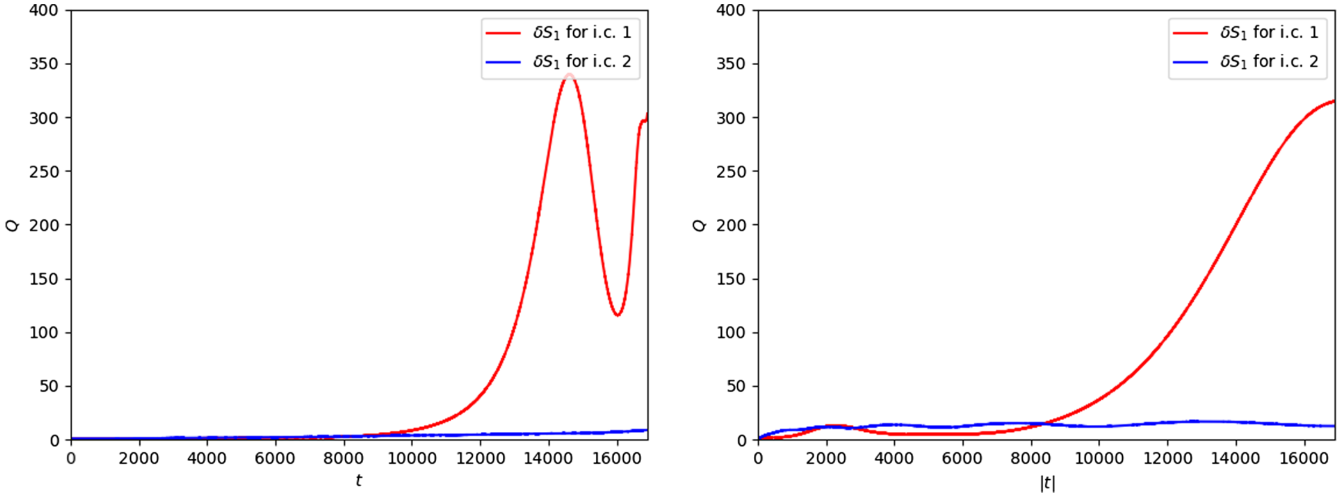

FIG. 9. These plots show Q vs t and vs $|t|$ for the two configurations shown in the previous table. The left plot correspond to a forward integration of the i.c. 1 and 2 staring from $\omega = 0.01$ to $\omega_{\max}$, while the right plot is a backward integration in time starting from the i.c. at t_m.

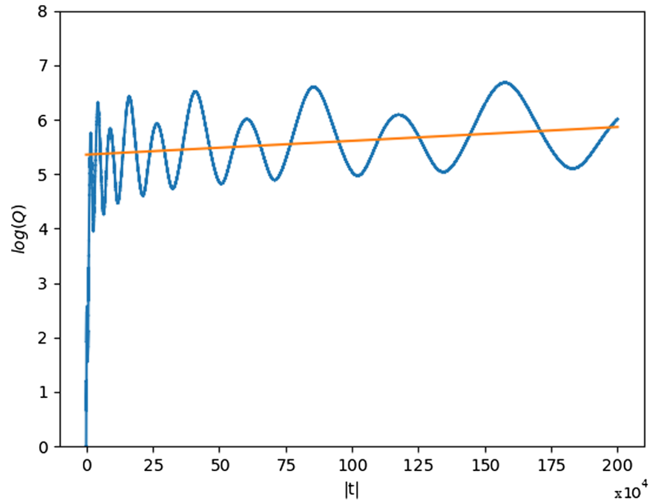

FIG. 10. This figure shows $\ln(Q)$ vs $|t|$, the orange curve corresponds to the least-squares fit to the simulation data. The slope of this curve is equal to the principal Lyapunov exponent 0.25×10^{-6}.

A similar situation arises when the spins are not strictly perpendicular to the plane of motion but their z components are parallel or antiparallel. (See Fig. 5).

Finally, and for completeness, we show two configurations (Fig. 6) where the spins are perpendicular to the orbital angular momentum.

B. One spinning black hole

In this subsection, we explore the presence of chaos when one of the BHs has no spin (see Fig. 7).

It is possible to note similar patterns, with chaotic regions, when the S_{1z} component is equal to zero (see Fig. 8 left).

We give some remarks.

(i) The nonspinning binary system is not expected to be chaotic. This is difficult to see around the origin of the right Fig. 8 since the parameter space is very dense. To explicitly show the stability of the nonspinning situation, we blow up the region near the origin, where one can clearly see in the right Fig. 8 that it is stable around the origin.

(ii) The system of ODEs is axially symmetric when only one spin is present; i.e., one can rotate the coordinate system around L_N and evolve an equivalent system. However, the same is not true for a perturbation of the initial configuration since the tangent space of the initial configuration breaks the axial symmetry. This can be seen in the left Fig. 8, where the perturbation is assumed to be in a given fixed direction.

(iii) Is is then clear that if the perturbation is aligned with the initial spin direction, then we should recover the axial symmetry in the Q factor. This is precisely what is found, and it is also shown in the right Fig. 8.

(iv) The one spinning binary system exhibits chaotic behavior when the initial spin is antialigned or perpendicular to L_N [28]. Since the evolution equations are very similar to the 2PN counterpart, we conclude that the 3.5PN equation of the angular frequency ω is responsible for this chaotic behavior.

C. Backward evolution

The systems used to make all the plots shown in the previous subsection evolve from zero to t_m, the time where the stop condition $\omega_{\max} = 0.05$ is reached. However, we can learn more about the dynamics of the PN equations by taking the final state of each configuration, and integrating backwards in time. The main idea is to show that for those systems with higher values of Q, it is not possible to determine exactly which initial state in the past yields the present configuration.

Consider the following initial conditions taken from the left Fig. 2:

Variables	i.c. 1	i.c. 1 at t_m	i.c. 2	i.c. 2 at t_m
ω	0.01	0.0500019587	0.01	0.0500012263
S_{1x}	0.2	0.0657547554	−0.2	0.4349953815
S_{1y}	0.08	0.9695664717	−0.08	−0.8451547904
S_{1z}	1.0	0.3194012666	1.0	0.3780111087
S_{2x}	1.0	0.6891034679	1.0	−0.0399506652
S_{2y}	0.0	−1.2349582589	0.0	1.4013884549
S_{2z}	−1.0	0.0038091043	−1.0	0.1857803617
$\hat{L}_{Nx}$	0.0	0.2084716645	0.0	0.3886283754
$\hat{L}_{Ny}$	0.0	0.4508028070	0.0	−0.8345210881
$\hat{L}_{Nz}$	1.0	0.8679380129	1.0	0.3905669460

These initial conditions have the same spin module, but they were chosen from two different regions. In the last table, the i.c is ordered from highest to lowest Q from left to right, respectively.

Now, we will perturb S_{1x}, S_{1y}, and S_{1z} by 10^{-9} simultaneously in order to emulate an indeterminacy in the measurement of S_1. Then, we evolve back in time and compute the Q factor; the results of these simulations are shown in the following figure (Fig. 9):

We interpret the red plot on the right in the following way: taking any initial time in the past, for example, $t \approx 17000$ (around 65 yr.), two very different configurations at that time yield the same final configuration at time t_m. On the other hand, the blue plot appears have evolved from essentially a unique configuration 65 years ago. Note the quotient Q is higher in the chaotic zone (i.c. 1) than i.c. 2 as is expected. This indicates that it is possible to find a data width where all these conditions arrive essentially at the same final state, that is, the same final point is in the solution space.

Finally, we run a long simulation of the i.c. 1 in order to compute the Lyapunov exponent. The result of this simulation is shown in the following figure (Fig. 10):

In the last figure, we go back around 7750 years, and how can we see, the slope of the orange curve gives a positive value $\lambda = 0.25 \times 10^{-6}$, indicating the presence of chaos in the system. Although this value seems small, because there is no stop condition, in a backward evolution it is possible to go back to longer times; so if we go back a few million of years, a small λ will become highly relevant and would lead to a large separation between $\mathbf{y}$ and the perturbation $\mathbf{y} + \delta\mathbf{y}$. In others words, the chaotic behavior will be more noticeable.

VI. FINAL REMARKS

In this article, we have studied the coalescence of spinning BHs in the adiabatic regime searching for the presence of chaos. Any chaotic behavior in this regime is passed on to the final inspiral period, and it can greatly reduce the possibility of detection even with templates that include spin effects. We thus focused on the stability of the spins in the binary system.

Using a numerical algorithm, we have performed many simulations in order to sweep the solution space for different mass ratios. We study the presence of chaos using the Lyapunov exponent. In particular, the Lyapunov time t_L is defined and compared with t_m, the maximum time of the computation associated with $\omega_{\max}$.

Our simulations show the existence of a large number of situations where the solution space contains chaos. As a matter of fact, only very symmetric situations with aligned spins do not exhibit chaotic behavior. Although the spin correlations of black hole binaries are not completely known at this time [29], it is very likely that massive amounts of points in the parameter space will be needed to provide the templates in order to detect weak sources of gravitational radiation.

Another important observation can be made by integrating the PN equations backwards in time for a long period. Since one finds positive Lyapunov coefficients for certain spin configurations, it then follows that there exists a wide range of BH spin configurations in the past which will reach the same spin configuration at t_m. This fact becomes relevant when trying to reconstruct the initial spin configuration of the BH binary at a distant past from the knowledge of the detected gravitational wave and final spin location of the remnant.

---

[1] LIGO Scientific Collaboration, Observation of Gravitational Waves from a Binary Black Hole Merger, Phys. Rev. Lett. **116**, 061102 (2016).

[2] N. J. Cornish and J. Levin, Comment on "Ruling Out Chaos in Compact Binary Systems", Phys. Rev. Lett. **89**, 179001 (2002).

[3] X. Wu and Y. Xie, Resurvey of order and chaos in spinning compact binaries, Phys. Rev. D **77**, 103012 (2008).

[4] J. Levin, Chaos and order in models of black hole pairs, Phys. Rev. D **74**, 124027 (2006).

[5] X. Wu and Y. Xie, Revisit on ruling out chaos in compact binary systems, Phys. Rev. D **76**, 124004 (2007).

[6] M. D. Hartl and A. Buonanno, Dynamics of precessing binary black holes using the post-newtonian approximation, Phys. Rev. D **71**, 024027 (2005).

[7] Y. Wang and X. Wu, Next-order spin-orbit contributions to chaos in compact binaries, Classical Quantum Gravity **28**, 025010 (2011).

[8] The Compute Unified Device Architecture, CUDA, http://developer.nvidia.com.

[9] T. Damour, Coalescence of two spinning black holes: An effective one-body approach, Phys. Rev. D **64**, 124013 (2001).

[10] T. Damour, P. Jaranowski, and G. Schaefer, Effective one body approach to the dynamics of two spinning black holes with next-to-leading order spin-orbit coupling, Phys. Rev. D **78**, 024009 (2008).

[11] Y. Pan, A. Buonanno, A. Taracchini, L. E. Kidder, A. H. Mroué, H. P. Pfeiffer, M. A. Scheel, and B. Szilágyi, Inspiral-merger-ringdown waveforms of spinning, precessing black-hole binaries in the effective-one-body formalism, Phys. Rev. D **89**, 084006 (2014).

[12] A. Gopakumar and C. Königsdörffer, Deterministic nature of conservative post-newtonian accurate dynamics of compact binaries with leading order spin-orbit interaction, Phys. Rev. D **72**, 121501 (2005).

[13] L. Blanchet, Gravitational radiation from post-newtonian sources and inspiralling compact binaries, Living Rev. Relativity **17**, 2 (2014).

[14] A. Buonanno, Y. Chen, and M. Vallisneri, Detecting gravitational waves from precessing binaries of spinning compact objects: Adiabatic limit, Phys. Rev. D **67**, 104025 (2003).

[15] Y. Pan, A. Buonanno, Y. Chen, and M. Vallisneri, Physical template family for gravitational waves from precessing binaries of spinning compact objects: Application to single-spin binaries, Phys. Rev. D **74**, 029905 (2006); Erratum, Phys. Rev. D **69**, 104017 (2004).

[16] M. Boyle, D. A Brown, L. E. Kidder, A. H. Mroué, H. P. Pfeiffer, M. A. Scheel, G. B. Cook, and S. A. Teukolsky, High-accuracy comparison of numerical relativity simulations with post-Newtonian expansions, Phys. Rev. D **76**, 124038 (2007).

[17] M. Hannam, S. Husa, B. Bruegmann, and A. Gopakumar, Comparison between numerical-relativity and post-Newtonian waveforms from spinning binaries: The orbital hang-up case, Phys. Rev. D **78**, 104007 (2008).

[18] L. E. Kidder, Coalescing binary systems of compact objects to post$^{5/2}$-Newtonian order v. spin effects, Phys. Rev. D **52**, 821 (1995).

[19] J. C. Butcher, *Numerical Methods for Ordinary Differential Equations*, 2nd ed. (John Wiley & Sons, Chichester, England, 2008).

[20] J. R. Dormand and P. J. Prince, A family of embedded Runge-Kutta formulae, J. Comput. Appl. Math. **6**, 19 (1980).

[21] M. Mahooti, Runge-kutta-fehlberg (rkf78), MATLAB Central File Exchange, https://www.mathworks.com/matlabcentral/fileexchange/61130-runge-kutta-fehlberg-rkf78 (2019).

[22] The Compute Unified Device Architecture CUDA, http://developer.nvidia.com.

[23] G. D. Quiroga, Malbec: A new CUDA-C ray-tracer in general relativity, Gen. Relativ. Gravit. **50**, 75 (2018).

[24] F. Herrmann, J. Silberholz, M. Bellone, G. Guerberoff, and M. Tiglio, Integrating post-Newtonian equations on graphics processing units, Classical Quantum Gravity **27**, 032001 (2010).

[25] S. Wiggins, *Introduction to Applied Nonlinear Dynamical Systems and Chaos* (Springer Science & Business Media, New York, USA, 2003), Vol. 2.

[26] S. H. Strogatz, *Nonlinear Dynamics and Chaos: With Applications to Physics, Biology, Chemistry, and Engineering* (Westview Press, Boulder, Colorado, USA, 2014).

[27] C. Skokos, The lyapunov characteristic exponents and their computation, in *Dynamics of Small Solar System Bodies and Exoplanets* (Springer, Berlin, Heidelberg, 2010), pp. 63–135, https://doi.org/10.1007/978-3-642-04458-8_2.

[28] X. Wu and G. Huang, Ruling out chaos in comparable mass compact binary systems with one body spinning, Mon. Not. R. Astron. Soc. **452**, 3167 (2015).

[29] S. S. Bavera, T. Fragos, Y. Qin, E. Zapartas, C. J. Neijssel, I. Mandel, A. Batta, S. M. Gaebel, C. Kimball, and S. Stevenson, The origin of spin in binary black holes predicting the distributions of the main observables of advanced LIGO, Astron. Astrophys. **635**, A97 (2020).